Epitaxially-grown Silicon Nanowires with a Gold

Molecular Adhesion Layer for Core/Shell Structures with

Compact Mie and Plasmon Resonances

Corban G. E. Murphey, Jin-Sung Park, Seokhyoung Kim, and James F. Cahoon*

Department of Chemistry, University of North Carolina at Chapel Hill, Chapel Hill, North Carolina 27599-3290, United States

ABSTRACT

Noble metal plasmonic nanostructures have attracted much attention because they can support deep-subwavelength optical resonances, yet their performance tends to be limited by high Ohmic absorption losses. In comparison, high-index dielectric materials can support low-loss optical resonances but do not tend to yield the same subwavelength optical confinement. Here, we combine these two approaches and examine the dielectric-plasmonic resonances in dielectric/metal core/shell nanowires. Si nanowires were grown epitaxially from (111) substrates, and direct deposition of Au on these structures by physical vapor deposition yielded non-conformal Au islands. However, by introducing a molecular adhesion layer prior to deposition, cylindrical Si/Au core/shell nanostructures with conformal metal shells were successfully fabricated. Examining these structures as optical cavities using both optical simulations and experimental extinction measurements, we found that the structures support Mie resonances with quality factors enhanced up to ~30 times compared to pure dielectric structures and plasmon

resonances with optical confinement enhanced up to ~5 times compared to pure metallic structures. Interestingly, extinction spectra of both Mie and plasmon resonances yield Fano lineshapes, whose manifestation can be attributed to the combination of high quality factor resonances, Mie-plasmon coupling, and phase delay of the background optical field. This work demonstrates a bottom-up synthetic method for the production of free-standing, cylindrically-symmetric semiconductor/metal core/shell nanowires that enables the efficient trapping of light on deep subwavelength length scales for varied applications in photonics and optoelectronics.

KEYWORDS. plasmonics, photonics, Mie resonance, vapor-liquid-solid mechanism, nanowire, core/shell structure.

Plasmonic materials can confine and guide light on a deep sub-wavelength length scale for diverse applications in sensing, ¹⁻³ catalysis, ⁴⁻⁶ and nano-optics. ⁷⁻⁹ However, their performance can be limited by large Ohmic absorption losses, ¹⁰ as many plasmonic materials are made with metals, resulting in often undesirable heating effects, large linewidths, and short surface plasmon polariton propagation distances. ¹¹ In comparison, dielectric materials have substantially lower losses and can sustain narrow linewidths and long propagation distances, but they are not generally able to confine light on the same sub-wavelength scale. ¹² Dielectric nanostructures, including Si nanowires (NWs), have attracted attention for their myriad photonic properties, ¹³⁻¹⁵ including the ability to trap and guide light and their potential to integrate with existing complementary metal oxide semiconductor (CMOS) device technologies. ¹⁶⁻¹⁸ Nanostructures designed with both dielectric and metallic materials such that a substantial fraction of the electric field intensity is preferentially localized within a dielectric region are a potential strategy to

achieve deep-subwavelength confinement of incident light with lower loss, thereby combining the advantages of both materials.

There are numerous reports of all-semiconductor core/shell NWs, $^{19-22}$ all-metal core/shell NWs, $^{23-25}$ and metal/semiconductor core/shell NWs. $^{26-31}$ Despite the conceptual simplicity of a cylindrical dielectric wire with a conformal metal shell, there are relatively fewer experimental studies of high aspect ratio semiconductor/metal core/shell NWs, and the reports typically consist of an Ω -shaped shell $^{32-36}$ vs. a conformal, cylindrically-symmetric shell. 37 Nevertheless, these Ω -shaped metallic shells have sparked interest recently, having been used to demonstrate a variety of optoelectronic effects: increases in photocatalytic activity via localized heating, 35 optical invisibility, 36 improved light absorption via metallic gratings, 38 enhanced electro- and photoluminescence and photocurrent from a plasmonic cavity, 39 second-harmonic generation and waveguiding, 40 plasmon-Mie resonances, 41 *et al.* For conformal metallic shells, there are several examples of semiconductor/metal and insulator/metal core/shell nanoparticles (NPs), $^{42-43}$ as well as Si NWs with Au shells deposited via the solution phase to create structures that support longitudinal plasmon resonances. 37

Here, we fabricated free-standing Si/Au core/shell NWs with arbitrarily high aspect ratio, conformal, cylindrically symmetric shells, and well-defined, uniform geometries via a bottom-up growth process. Using finite-element method (FEM) optical simulations combined with experimental extinction measurements, we demonstrate that these core/shell NWs yield Mie resonances that are blue shifted with a dramatic enhancement of the radiative Q-factor relative to structures without a metallic shell and yield dipolar and quadrupolar plasmon resonances substantially more confined relative to structures without a semiconductor core. Moreover, the thickness of the metallic shell mediates a trade-off between the capacity for resonances to trap

light and to couple to an external plane wave. This understanding of Mie and plasmon resonances in dielectric/metal core/shell nanowires could enable new photonic and optoelectronic applications of these resonances.

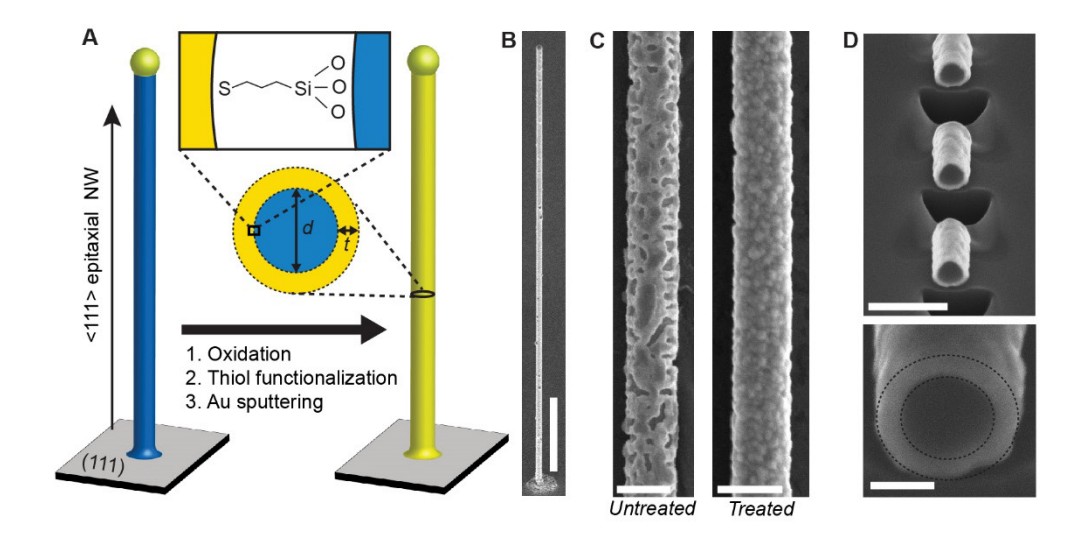


Figure 1. Si/Au core/shell NW fabrication. (A) Schematic of the fabrication process. Insets: schematic of the NW with a Si core diameter *d* and Au shell thickness *t* and schematic of surface functionalization by 3MPTES. (B) Tilt view SEM image of an epitaxial core/shell NW still attached to the (111) substrate; scale bar, 5 μm. (C) SEM image of core/shell NWs without surface treatment (left) and with 3MPTES surface treatment (right); scale bars, 250 nm. (D) Tilt-view SEM image (upper) of a representative core/shell NW showing periodic FIB milling to reveal the NW cross section (scale bar, 500 nm) and a magnified SEM image (lower) highlighting the Si/Au boundary (scale bar, 100 nm).

RESULTS AND DISCUSSION

Fabrication of cylindrically symmetric Si/Au NWs

As illustrated in Figure 1A, Si/Au core/shell NWs were fabricated by sequential epitaxial vapor-liquid-solid (VLS) growth of <111> oriented Si NWs, surface oxidation, molecular functionalization, and Au physical vapor deposition by sputtering. For epitaxial VLS growth, NWs were synthesized in home-built chemical vapor deposition (CVD) system following a procedure reported previously using Au NP catalysts to control the diameter (d) of the Si core.⁴⁴ NWs were subsequently oxidized via ozone, functionalized with (3mercaptopropyl)triethoxysilane (3MPTES) to promote metal adhesion (see Methods section), and sputter coated with Au metal to control the metal thickness (t). As shown by the scanning electron microscopy (SEM) image in Figure 1B, the process yields vertical, free-standing Si NWs coated with Au. Figure 1C compares the morphology of Au deposition on NWs with and without the 3MPTES functionalization, where a substantial density of pinholes is apparent without molecular functionalization, but functionalization results in a relatively smooth and continuous Au film. 3MPTES and related thiols have been shown to be effective, non-metal adhesion layers, 45-48 and in particular, Gothe et al. 48 demonstrated a (3mercaptopropyl)trimethoxysilane monolayer that enabled uniform Au film deposition on an oxidized Si substrate. We purposefully avoided conventional metallic adhesion layers such as Cr to avoid additional metals that may impact the plasmon resonances of the Au shell. The vaporphase functionalization we employed in this work was chosen over solution-based methods³⁷ because capillary forces would collapse the NWs. 49 As shown in Figure 1D, periodic focused ion beam (FIB) cross sectioning of a core/shell NW was performed, and the SEM images confirm the uniformity and conformality of the Au shell.

Figure 2 illustrates the general dielectric photonic and plasmonic characteristics of the core/shell NWs by comparing simulations on three structures: a cylindrical but hollow Au shell,

a hybrid Si/Au core/shell NW, and a Si NW. Figure 2A displays the frequency of relevant Mie and/or plasmon resonances in each of the structures for select geometric parameters under transverse electric (TE) polarization, and the corresponding magnetic field profiles and electric field profiles are shown in Figure 2B and Figure S1, respectively. The hollow Au shell of t = 30nm supports a magnetic dipolar plasmon resonance (DPR) and quadrupolar plasmon resonance (QPR) in the near-IR when the hollow core diameter is large, e.g. 730 nm. Field profiles demonstrate confinement primarily within the hollow core of the structure, but the optical confinement of the field is relatively minor, only $\sim \lambda/2$. The Si/Au core/shell NW supports the same plasmon resonances with t = 30 nm, but interestingly, resonances at similar near-IR frequencies are achieved with a Si core diameter (d = 150 nm) that is nearly 5 times smaller, as shown by the magnetic field profiles in Figure 2B. This reduction results from the high refractive index of Si,⁵⁰ allowing strong confinement in a subwavelength geometry. Without an Au shell, a Si NW of d = 150 nm supports TE₀₀ and TE₀₁ Mie resonances in the visible wavelength range,⁵¹ and the addition of an Au shell blue shifts the Mie resonance wavelengths while the general field profiles are retained. Figure 2C displays the extinction efficiency (Q_{ext}) spectra of the hollowcore Au, Si/Au, and Si nanostructures. Both Mie and plasmon resonances appear as distinct peaks in the Q_{ext} spectra and typically exhibit Fano-like characteristics, as will be discussed below.

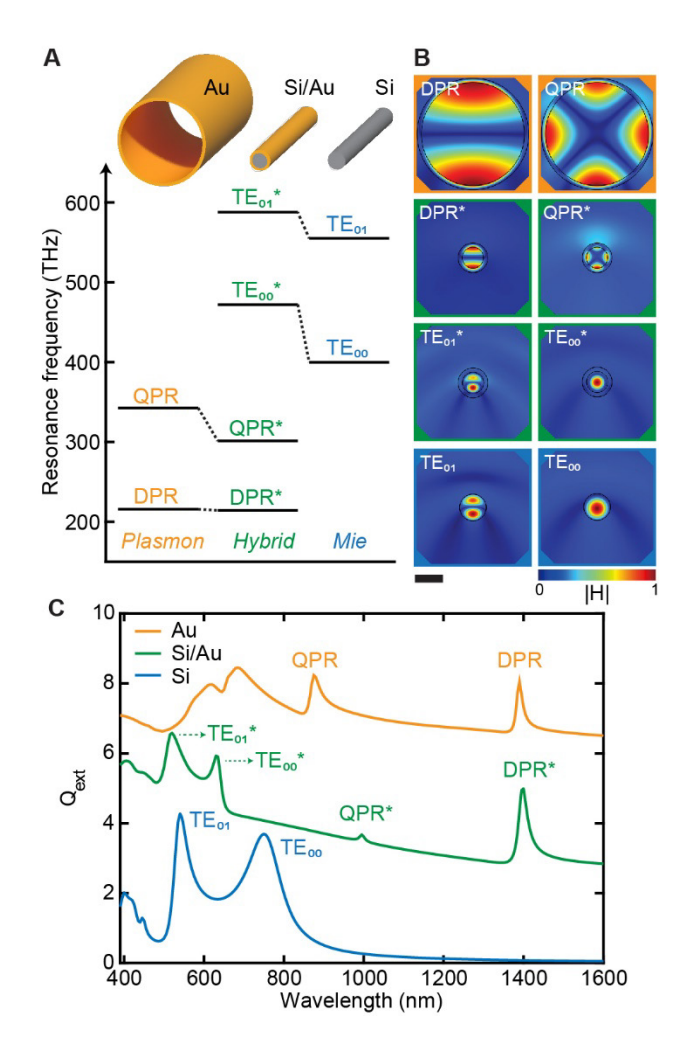


Figure 2. Comparison of simulated resonances in Si, Si/Au, and Au nanostructures. (A)

Frequency of resonances in a large (d = 730 nm; t = 30 nm) hollow Au nanotube (left), thin (d = 150 nm, t = 30 nm) Si/Au NW (center), thin (d = 150 nm) Si NW (right). Relative sizes of schematics are to scale. (**B**) Magnetic field spatial profiles of the Mie and plasmon resonances labeled in panel A; scale bar, 200 nm. (**C**) Simulated Q_{ext} spectra under TE polarization for the NWs depicted in panel A. Spectra are vertically offset by 2.5 units for clarity.

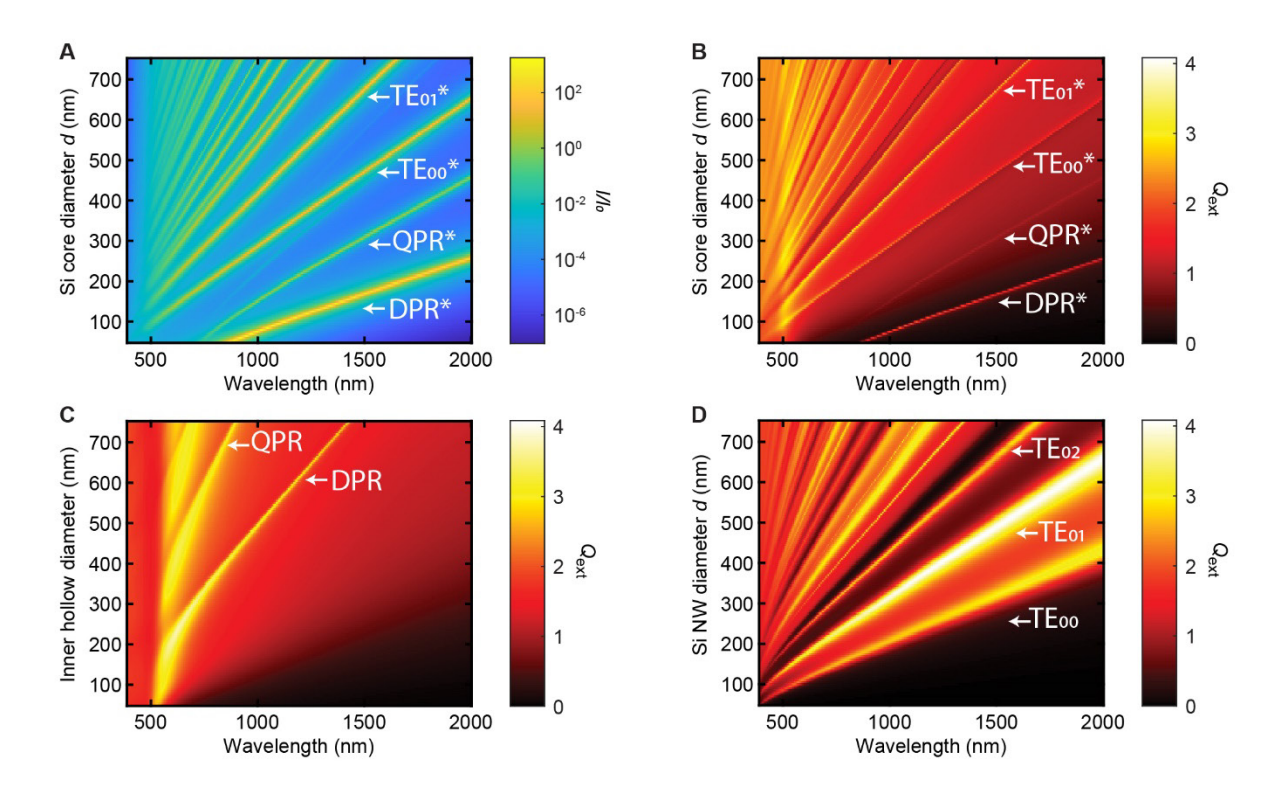


Figure 3. Diameter-dependent simulated optical properties of hollow Au, Si/Au core/shell, and Si NW structures. (A) Logarithmic heatmap of I/I_0 spectra for a Si/Au core-shell NWs with a t = 30 nm and varying Si core diameter d. (B) Heatmap of $Q_{\rm ext}$ spectra for Si/Au NWs corresponding to panel A. (C) Heatmap of $Q_{\rm ext}$ spectra for hollow Au structures with varying d and t = 30 nm. (D) Heatmap of $Q_{\rm ext}$ spectra for bare Si NWs of varying d.

To understand the effect of geometry on the Mie and plasmon resonances, optical simulations were performed on varying geometries by systematically changing d and t. Figures 3A and 3B display heatmaps showing the effect of varying d with a fixed t = 30 nm on the integrated electric field intensity enhancement, I/I_0 , spectra within the Si/Au NWs and the $Q_{\rm ext}$ spectra, respectively. Analogous $Q_{\rm ext}$ heatmaps of a hollow Au shell of t = 30 nm and of a bare Si NW are shown in Figures 3C and 3D, respectively. Each of the diagonal streaks on these heatmaps correspond to a plasmon or Mie resonance, and we focus here on the DPR, QPR, TE₀₀,

and TE₀₁ resonances. Several interesting trends are apparent from the data in Figure 3. For Mie resonances, the addition of the Au shell causes increasing blue shifts of the Mie resonance positions as d increases. For instance, with d = 150 nm, the TE₀₀ resonance shifts from 760 nm to 630 nm upon addition of the Au shell, but for d = 700 nm it shifts from 3400 nm to 2120 nm (based on a linear extrapolation of the data). Similarly, for DPR and QPR resonances in hollow Au shell and Si/Au NWs, the addition of the Si core causes increasing redshifts for the Si/Au structures with increasing d. For instance, with d = 150 nm, upon addition of the Si core, the DPR resonance shifts from a hardly discernable peak at 570 nm to 1400 nm, but for d = 700 nm shifts from 1340 nm to well into the IR, around 4.6 μ m (based on linear extrapolation).

The thickness (t) of the Au shell also has a dramatic effect on the resonances, and Figure 4A displays I/I_0 within the hybrid NW as a function of t (note logarithmic scale). As t increases from 1 nm to 100 nm, the spectral position and linewidth of both the DPR* and QPR* blue shift and narrow. Although the Mie resonances also shift, the effect is less dramatic compared to the plasmon resonances. However, as t increases, both the Mie and plasmons resonances show a decrease in I/I_0 and begin to disappear from the spectra. Fits of the DPR peaks to Lorentzian functions (see Supporting Information) illustrate several important trends. As shown in Figure 4B, the full width at half maximum (FWHM) decays exponentially with increasing t, and the peak amplitude of I/I_0 increases and then decreases with increasing t, reaching a maximum at $t \sim 30$ nm. As shown in Figure 4C, the peak shift as a function of t, $\Delta \lambda_{\rm DPR}(t)$ defined as $\lambda_{\rm DPR}(t) - \lambda_{\rm DPR}(t) = 100$ nm), and the peak area both decay approximately exponentially with increasing t. The trend in FWHM and amplitude suggest that increasing t improves the quality factor (Q factor) of the plasmon resonances by facilitating better trapping of light, leading to a narrowing of the linewidth and increase of the peak amplitude, as apparent in Figure 4B. However, the

trend in peak area in Figure 4C suggests that increasing t also decreases the ability of the cavity to couple to the external plane wave because less light penetrates the cavity, leading to a decrease in the overall energy coupled into the cavity. We also note that the skin depth of Au in the NIR is \sim 25 nm (Figure S2), which is consistent with a substantial change in Q factor and shift of the plasmon resonance peak positions for smaller values of t.

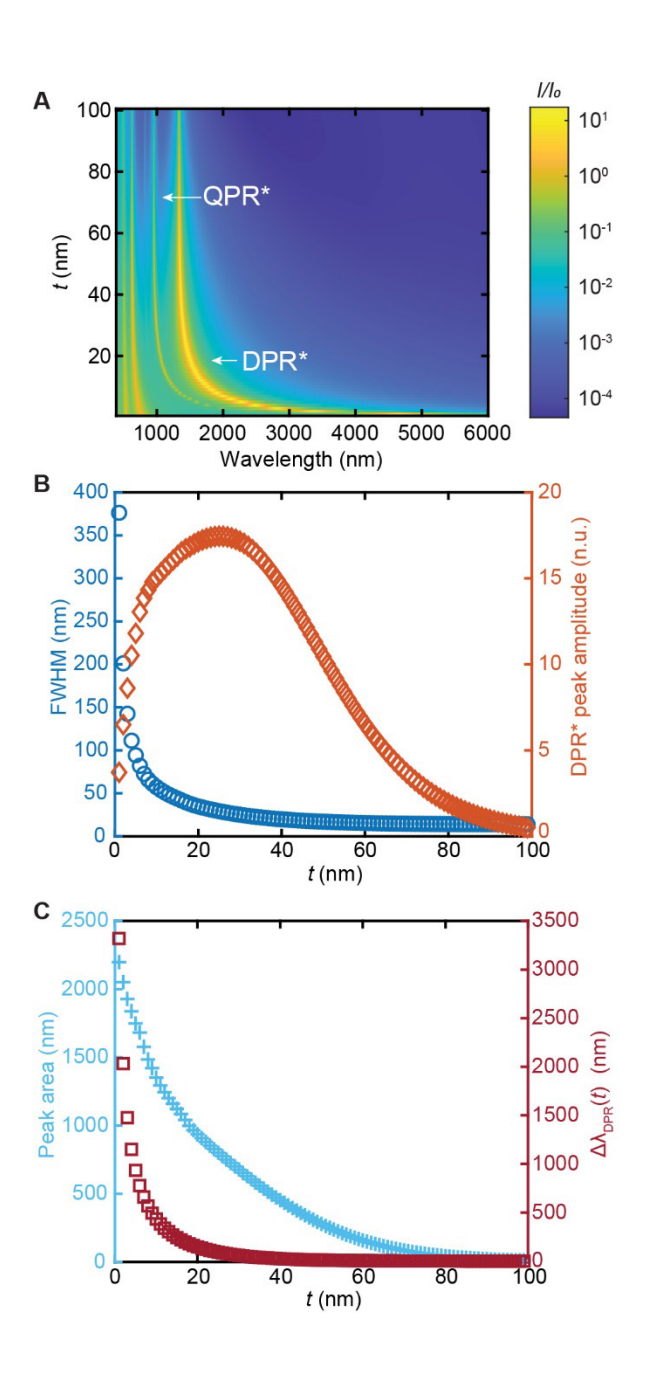


Figure 4. Thickness-dependent simulated optical properties of Si/Au core/shell NWs. (A) Logarithmic heatmap of I/I_0 spectra with a d = 150 nm Si core and varying t. (B) FWHM (blue circles, left-hand axis) and peak amplitude (orange diamonds, right-hand axis) of the DPR peak as a function of t. (C) Peak area (blue crosses, left-hand axis) and peak shift relative to peak position at t = 100 nm (red squares, right axis) for the DPR peak as a function of t.

To more robustly interpret the trends in the optical properties of Si/Au core/shell NWs, we used temporal coupled mode theory (TCMT) to fit scattering and extinction data. Previously, TCMT has been used to describe the interaction between bound states in the continuum and Mie resonances in geometric superlattice NWs, ¹⁵ and a similar approach is adopted here but with several modifications. Because the absorptive loss cannot be neglected in the plasmonic structures, the total decay rate, γ_{tot} , can be split into radiative and non-radiative components, γ_r and γ_{nr} , respectively, with $\gamma_{tot} = \gamma_r + \gamma_{nr}$. In addition, a phase term, φ , is implemented to account for the phase change of the outgoing wave after interaction with the nanostructure. Phase differences with the outgoing field have previously been discussed as the origin of Fano features in Mie scattering spectra ⁵² and individual semiconductor nanostrips. ⁵³ The TCMT expression is thus given by:

$$\frac{d}{dt}A_m^{Mie} = \left[-i\omega_m^{Mie} - \gamma_{r,m}^{Mie} - \gamma_{nr,m}^{Mie}\right]A_m^{Mie} + \kappa_m^{Mie}h_m^+,\tag{1}$$

with

$$h_m^- = e^{i\varphi} h_m^+ + d_m^{Mie} A_m^{Mie}, \tag{2}$$

where A_m^{Mie} , ω_m^{Mie} , $\gamma_{r,m}^{Mie}$, $\gamma_{nr,m}^{Mie}$ are the amplitude, frequency, radiative decay rate, and non-radiative decay rate of the hybrid Mie resonances of azimuthal order m, and h_m^+ and h_m^- are the amplitudes of the incoming and outgoing plane waves, respectively. The reflection coefficient R_m

is defined as h_m^-/h_m^+ . The $\gamma_{r,m}^{Mie}$ and $\gamma_{nr,m}^{Mie}$ decay rate terms are related to the radiative Q-factor (Q_r) and non-radiative Q-factor (Q_{nr}) by the general formula $Q=\frac{\omega}{2\gamma}$. The coupling coefficients to the incoming and outgoing waves are given by κ_m^{Mie} and d_m^{Mie} , respectively. Through time-reversal symmetry and energy conservation, $\kappa_m^{Mie}=d_m^{Mie}=i\sqrt{2\gamma_{r,m}^{Mie}}\,e^{\frac{i\varphi}{2}\cdot 15,\,54}$ The scattering efficiency, Q_{sca} , and absorption efficiency, Q_{abs} , of a NW⁵⁵ are:

$$Q_{sca} = \frac{\lambda}{2\pi r} \sum_{m=-\infty}^{\infty} \left| \frac{1 - R_m}{2} \right|^2, \tag{3}$$

and

$$Q_{abs} = \frac{\lambda}{4\pi r} \sum_{m=-\infty}^{\infty} 1 - |R_m|^2, \tag{4}$$

where λ is the wavelength and r is the NW radius. An analogous set of equations can also be written for the plasmon resonances.

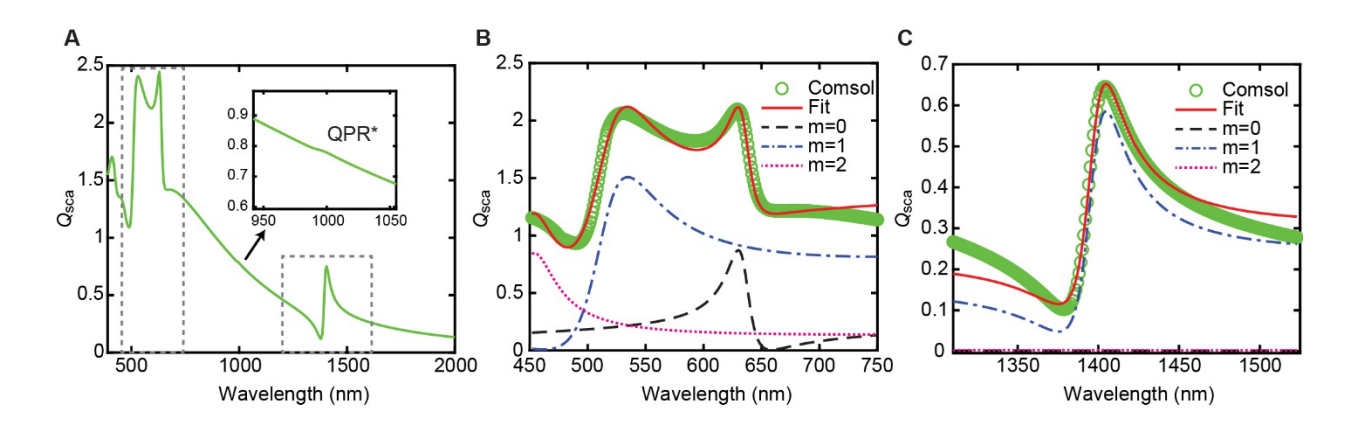


Figure 5. TCMT fitting of simulated scattering spectra from a Si/Au core/shell NW. (A)

 Q_{sca} spectrum for d=150 nm and t=30 nm. Dashed gray boxes denote the regions where TCMT fits were performed. Inset: magnified view of the spectral region corresponding to the QPR*. (**B**) TCMT fit of the Mie resonances from the Q_{sca} spectrum in panel A. (**C**) TCMT fit of the DPR resonance from the Q_{sca} spectrum in panel A.

A TCMT fit to the simulated scattering efficiency (Q_{sca}) spectrum of a d = 150 nm and t =30 nm Si/Au core/shell NW is shown in Figure 5. The simulated scattering spectrum in Figure 5A shows Fano-like features in the visible region and near 1400 nm, corresponding to Mie resonances and plasmon resonances, respectively. Note that compared to extinction efficiency (Q_{ext}) spectra, the QPR* resonance near 1000 nm is barely perceptible in the Q_{sca} spectrum because the intensity of the feature primarily results from Q_{abs} rather than Q_{sca} , where $Q_{ext} = Q_{abs}$ $+Q_{\rm sca}$. In the TCMT analysis, we assume for simplicity that φ is constant across the Mie or plasmon resonances individually fit by TCMT. We also assume that the full Q_{sca} spectrum is a linear combination of each angular channel m for each type of resonance, simplifying the fitting procedure. To support the TCMT analysis, we also performed eigenfrequency analysis to separately determine values of Q_r and Q_{nr} (see Methods and below) that can be used in setting initial parameters for γ_r and γ_{nr} , respectively. Representative TCMT fits of both the TE₀₀* (m = 0) and TE_{01}^* (m = 1) Mie resonances and the DPR* for the spectrum in Figure 5A are shown in Figure 5B and 5C, respectively. The TCMT analysis reasonably fits the simulations, indicating that the phase difference between Mie and plasmon resonances and the outgoing field can explain the asymmetric, Fano line shapes of each resonance. However, an alternate plausible explanation for the Fano lineshape is coupling between Mie and plasmon resonances. A TCMT fit of the DPR* data using a coupling term between resonances in the same angular channel m is also able to reasonably reproduce the DPR* features (see Supplemental Information and Figure S3). Thus, both a phase difference of the outgoing wave and coupling between Mie and plasmon resonances may be causes of Fano-like lineshapes. However, due to the relatively large energy difference between the Mie and plasmon resonances, we believe the phase difference is the

stronger contributor to the effect. Moreover, the observation of a Fano lineshape with TE_{00} modes yet the absence of an m = 0 plasmon resonance suggests that the phase difference is the better explanation for the Fano lineshape characteristics of the Mie resonances. A table enumerating the optimized parameters for this TCMT fitting is given in Table S1.

From the TCMT fits and eigenfrequency analysis, we can determine Q_r, Q_{nr}, and Q_{tot}, where $Q_{tot}^{-1} = Q_r^{-1} + Q_{nr}^{-1}$, and Q_{tot} yields the total Q factor that reflects the linewidth and amplitude observed in simulations and experiments (see Methods section). Figure 6 plots the Q factors for Mie and plasmon resonances as a function of geometric parameters, and all fit and eigenfrequency parameters are summarized in Tables S2-S4. For Mie resonances, Qtot for Si/Au structures dramatically increases with increasing d, changing from a value of ~ 10 to ~ 150 from d = 150 nm to 750 nm, respectively, as shown in Figure 6A. Moreover, both Q_{nr} and Q_r steadily increase as d increases. In comparison, Q_{tot} for Mie resonances of bare Si NWs are nearly constant with values of <10 across this diameter range. One may expect these trends to be the result of the redshift of the Mie resonances into the NIR, outside the range of Si absorption, but eigenfrequency calculations performed in the absence of Si absorption (i.e. $\kappa_{Si} = 0$) show nearly identical results (Figure S4A). Rather, when the thin Au shell surrounds the Si NW core, it acts as a mirror, reflecting back light that would otherwise leak out, 40 increasing the Q-factor compared to bare Si NWs. Furthermore, as the Si core diameter increases, the relative Si:Au volume fraction also increases, so a larger proportion of the electric field intensity of the resonance is located in the low-loss Si core, rather than in the Au shell (Figure S4B,C). This concentration of electric field leads to a narrower Mie resonance peak width in the I/I_0 spectra (Figure S5) as Si core diameter increases, consistent with the increasing Q factor.

For plasmon resonances, Q_{tot} dramatically increases with increasing t, plateauing at a value of ~80-100 for t values above ~60 nm, as apparent from Figure 6B. Eigenfrequency simulations, TCMT fits of simulated scattering spectra, and Lorentzian fits of I/I_0 peaks all produce similar values and trends in Q factor. Interestingly, eigenfrequency analysis indicates that Q_r is >100 for all t values and increases to as high as 10^5 for t = 100 nm. Thus, Q_{tot} is almost entirely limited by the non-radiative component, Q_{nr} , whereby an increasing t acts as an increasingly efficient mirror for retaining light in the Si core, which increases Q_r , but at the expense of adding an increasing volume of lossy Au to the structure. The Si/Au core/shell NW design thus offers a good quality plasmon resonance, as prior reports of the Q factors of plasmon modes in metal/semiconductor hybrid nanostructures have yielded values ranging from approximately 10 to $250.^{56-57}$

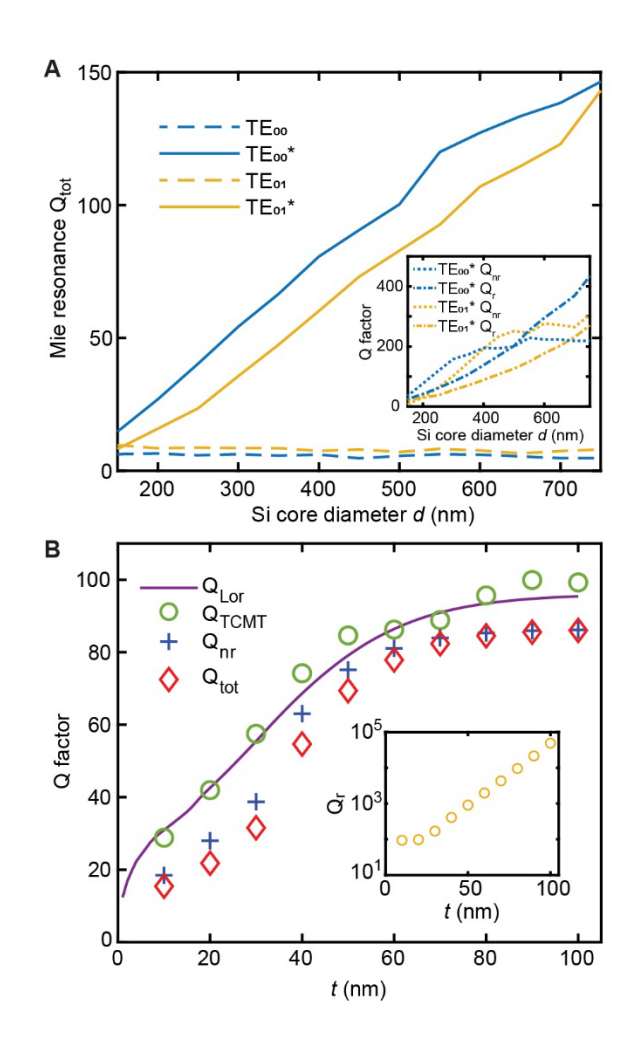


Figure 6. Changes in Q factor with changing geometry. (A) Total Q factors for TE_{00} and TE_{01} Mie resonances determined from eigenfrequency analysis as a function of d of bare Si NWs (dashed lines) and Si/Au core/shell NWs with fixed t = 30 nm (solid lines). Inset: Plot of Q_r (dot-dashed line) and Q_{nr} (dotted line) of the TE_{00} * (blue) and TE_{01} * (yellow) Mie resonance. (B) Q factors as a function of t for the DPR of a Si/Au core/shell NW with fixed d = 150 nm. Q factors were determined from Lorentzian fits of I/I_0 (labeled Q_{Lor} , solid purple line), TCMT fits of Q_{sca} spectra (labeled Q_{TCMT} , green circles), and eigenfrequency analysis, giving Q_{nr} (blue plus sign) and Q_{tot} (red diamonds). Inset: Q_r (yellow circles) determined by eigenfrequency analysis.

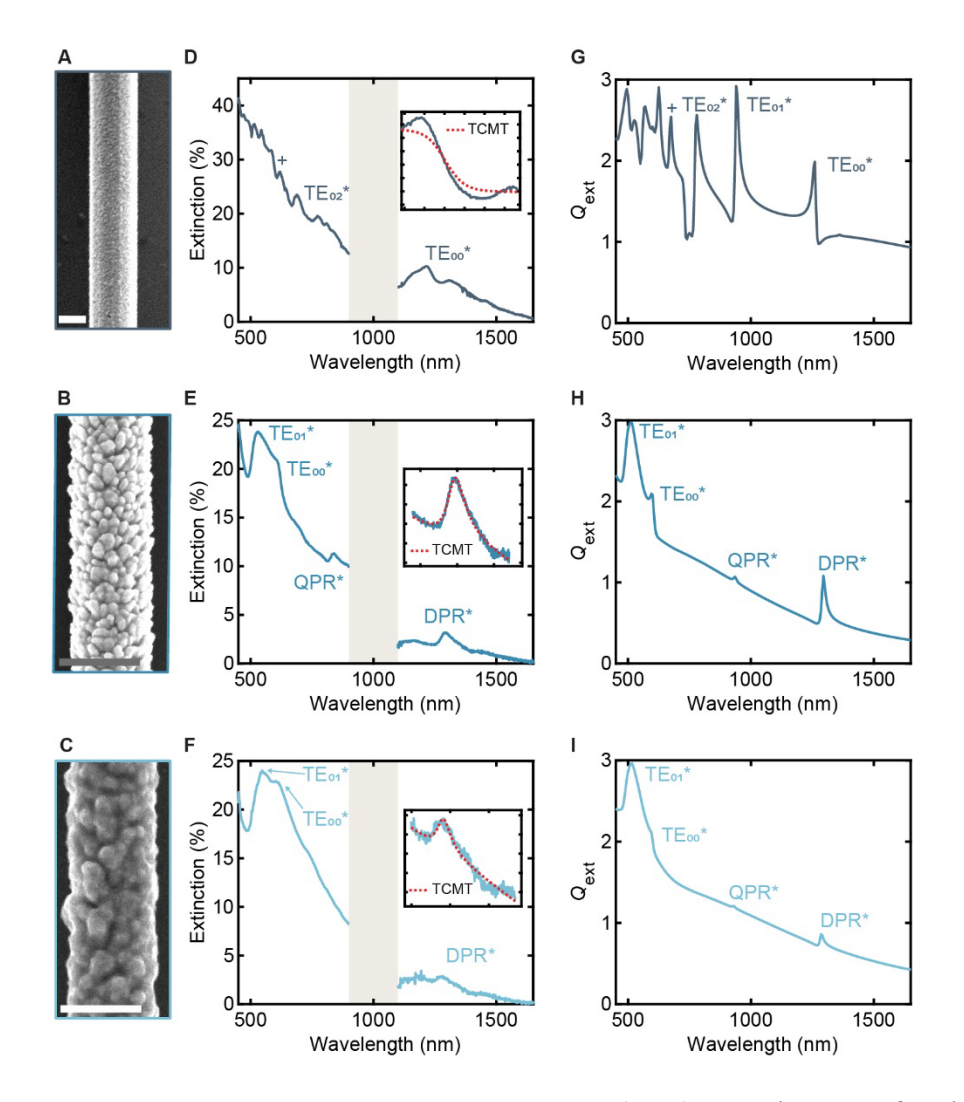


Figure 7. Experimental detection of hybrid resonances. (A-C) SEM images of a Si/Au core/shell NWs with d = 385 nm and t = 30 nm (panel A), d = 174 nm and t = 47 nm (panel B), and d = 162 nm and t = 65 nm (panel C); all scale bars, 250 nm. (**D-F**) Experimental visible and near IR spectra of the Si/Au core/shell structures with spectra in panels D-F corresponding to the SEM images in panels A-C. (**G-I**) Simulated Q_{ext} spectra of Si/Au core/shell structures with d = 385 nm and t = 30 nm (panel G), d = 140 nm and t = 50 nm (panel H), and d = 140 nm and t = 70 nm (panel I). Shaded regions from 950 to 1100 nm in the experimental spectra denote an inaccessible spectral region due to experimental limitations.

Experimental extinction measurements were performed using a home-built, polarization-controlled extinction microscope described previously¹⁴ by transferring core/shell NWs from the growth substrate to microscopy slides. For experimental analysis, we targeted a NW with large diameter and thin shell (d = 400 nm, t = 30 nm) and a small diameter NW (d = 150 nm) with thin (t = 30 nm) and thick (t = 50 nm) Au shells. SEM images of the experimentally measured NWs are shown in Figures 7A-C, with corresponding experimental extinction spectra and simulated spectra shown in Figures 7D-F and Figure 7G-I, respectively. SEM images were used to deduce the exact geometric dimensions of each core/shell NW. Optical simulations were performed on the approximate geometries observed experimentally, and reasonable agreement was observed between the experimental and simulated spectra, allowing the assignment of Mie and plasmon resonances by comparison of the spectra.

In Figure 7D, a TE₀₀* Mie resonance is observed in the NIR at 1250 nm for a $d \approx 385$ nm and $t \approx 30$ nm NW, and the resonance exhibits the expected asymmetric, Fano-like lineshape. The visible spectrum has a high density of resonances resulting from multiple Mie resonances supported in the visible range for this diameter. In Figure 7E, TE₀₀*, TE₀₁*, QPR*, and DPR* resonances are all clearly observed for a $d \approx 170$ nm and $t \approx 45$ nm NW. Finally, in Figure 7F, TE₀₀* and TE₀₁* resonances are observed in a NW with a similar core diameter, $d \approx 160$ nm, but with a thicker Au shell of $t \approx 65$ nm. The QPR* intensity has decreased enough to be unresolvable, perhaps cloaked, ³⁶ consistent with simulated spectrum in Figure 7I. Similarly, the DPR* is again observed in the NIR, and its spectral position is largely unchanged compared to the thinner Au shell but the intensity is decreased.

We fit the experimental extinction spectra using our TCMT model for $Q_{\rm ext}$ including an additional linear background to account for a slowly varying background. All fitted parameters

are summarized in Table S5. When the TE_{00}^* resonance in Figure 7D is fit with TCMT, a reasonable fit is achieved with a Q_{tot} of ~20 Similarly, the experimental DPR* spectrum in Figure 7E is reproduced well with a Q_{tot} of 22.3. Finally, the DPR* in Figure 7F is fit with a Q_{tot} of ~30. The experimental values of Q_{tot} are 3-4 times lower than the theoretical values determined by TCMT fits of the simulated spectra. Considering the roughness of the Au shell, ⁵⁷ presence of oxide and organic layers at the Si/Au interface, finite beam spot size, and finite NW lengths that could introduce additional losses and changes to the resonances, we consider these Q-factors to be in reasonable agreement with simulations. Moreover, the thicker Au shell produces a Q factor ~50% higher, in agreement with expectations from simulations. Thus, the experimental results confirm the ability to fabricate core/shell nanostructures with higher Q factor Mie resonances and high Q factor and confined plasmon resonances.

CONCLUSION

In summary, we have demonstrated a hybrid Si/Au core/shell NW with hybrid Mie and plasmon resonances. We synthesized the hybrid NWs by combining VLS Si NW growth with 3MPTES surface functionalization and Au sputtering. Experimental extinction spectra of hybrid NWs agree well with simulations, and analysis of the hybrid plasmonic and photonic properties of the NWs by TCMT demonstrates they are easily tuned by modifying core diameter *d* and shell thickness *t*. The high-index Si core of the hybrid NW allows for NIR plasmon resonances to exist in a much smaller structure in comparison to a simple hollow Au nanoshell with minimal reduction in Q-factor. Hybrid Mie resonance Q-factors are also greatly enhanced, especially in larger NWs. Phase-modified TCMT fitting results are in good agreement with simulated scattering and experimental extinction, demonstrating that although Mie-plasmon coupling likely

contributes, the phase of background field also plays a primary role in observed Fano lineshapes. This bottom-up hybrid NW synthesis could be altered to include different NW materials, such as Ge and SiO₂, and different metals, such as Cu, Al, and Ag, with similar predicted results and trends (Figure S6). Numerous potential optoelectronic applications could be considered, including core-shell NW-based photodetectors,³⁶ core/shell NW array sensors,⁵⁸ or NW-based solar energy devices⁵⁹ with plasmonically-enhanced infrared light absorption.³⁸

MATERIALS AND METHODS

Epitaxial Si NW growth. Silicon nanowires were grown in a home-built, hot-wall chemical vapor deposition system with silane (SiH₄; Voltaix), hydrogen chloride (HCl anhydrous; Matheson TriGas; 5 N semiconductor grade), and hydrogen (H₂; Matheson TriGas; 5 N semiconductor grade) in a 1-inch quartz-tube furnace (Lindberg Blue M). To prepare growth substrates, p-type Si (111) wafers (Nova Electronic Materials; B-doped; 1-10 Ω·cm) were cleaned by sonication in acetone (Fisher Scientific), isopropyl alcohol (IPA; Fisher Scientific), and water and placed in a UV/O₃ cleaner (Samco UV-1) for 5 minutes. Substrates were briefly immersed in buffered hydrofluoric acid (BHF; Transene BHF Improved) for native oxide removal, and Au nanoparticle deposition was performed in a solution containing 5 parts of prediluted Au colloid solution (Ted-Pella; 150 nm or 400 nm) and 1 part BHF. Au-functionalized substrates were then treated by UV/O₃ for removal of residual organics, then by BHF for removal of native oxide just prior to placement in the tube furnace. All NWs were nucleated at 480 °C with 2 standard cubic centimeters per minute (sccm) of SiH₄, 4 sccm of HCl, and 196 sccm of H₂ at 2 Torr total reaction pressure for 60 minutes. These conditions were then

maintained for an additional 14 hours, yielding epitaxial Si NWs \sim 28 μm in length (see Figure S7).

Molecular functionalization and Au deposition. As-synthesized epitaxial Si NW growth chips were placed in an ozone cleaner for 5 minutes at 150 °C to develop a thin, stable oxide layer to promote 3MPTES adhesion to the Si NW surface. The oxidized epitaxial Si NW growth chips and a small glass well filled with 200 μL of 3MPTES (Sigma) were placed in a glass petri dish in a vacuum oven (Fisher Scientific Isotemp 280A). The pressure in the vacuum oven was reduced to -30 inHg relative to atmosphere, and held for 30 minutes. Then, the vacuum valve was closed, and temperature was increased to 60 °C for 90 minutes. Sputtering was then used to deposit approximately 30 nm of Au onto the NW surface (Kurt Lesker PVD 75) at a rate of 1 Å/s. To account for anticipated shadowing effects during the sputtering process, the target thickness was 150 nm for the NWs in Figure 7A-B and 200 nm for the NW in Figure 7C.

Focused ion beam milling and SEM imaging. Au/Si NWs were mechanically contact-transferred onto p-type Si (111) wafers (Nova Electronic Materials; B-doped; 1-10 Ω ·cm), which had been cleaned as described above. Cleaning cross-section cuts were made on the NWs using a 1.5 pA current using a FEI Helios 600 Nanolab Dual Beam System. All SEM imaging was conducted on the same system.

Extinction measurements. Au/Si NWs were mechanically contact-transferred onto standard glass microscopy slides (Fisher Scientific) which were coated with ~3 nm of ITO by sputtering (Kurt Lesker PVD 75) to facilitate SEM imaging. Prior to NW transfer, the slides were cleaned by sonication in acetone and IPA, then blown dry with N₂ and placed in a O₃ cleaner for 5 minutes at 150 °C. Extinction was measured with a supercontinuum laser (NKT Photonics; SuperK Extreme EXB-6) after passing through a monochromator (Princeton

Instruments; Acton SP2300) to output a single wavelength with < 2 nm bandwidth. The laser was collimated into a beam size of ~1 mm, linearly polarized by a Glan-Thompson polarizer, and split evenly into a reference and probe beam, each of which were collected by reflective fiber couplers (Thorlabs; RC04FC-P01) for balanced detection with a Nirvana balanced photoreceiver [Newport; Nirvana Auto-Balanced Photoreceiver 2007 (visible) or 2017 (NIR)]. The probe beam was directed through a pair of matched reflective objectives (Thorlabs; LMM-40X-P01/UVV; numerical aperture 0.50), through one side of the back aperture of the first objective in order to deeply under-fill the aperture and achieve quasi-plane wave illumination of an isolated NW with a low effective numerical aperture and a beam spot size of ~10 μ m. The optical power was collected with the probe beam placed on and off the NW by modulating the substrate position using a piezo positioner (Mad City Labs; Nano-LP 200). Measured extinction (%) was calculated as $(1-T) \times 100$ with $T = P/P_0$, where P and P_0 are transmitted powers collected with the beam on and off the NW, respectively.

Finite element simulations. Finite-element optical simulations were performed using COMSOL Multiphysics. For 2D plane wave and eigenfrequency calculations, NWs were embedded in air, surrounded by a perfectly matched layer (PML). The air surrounding the NW was terminated by a scattering boundary. The scattering cross-section, σ_{sc} , was calculated by integrating Poynting vectors across the outer surface of the NW in all directions and dividing by the optical power incident on the NW. The absorption cross-section, σ_{abs} , was calculated by integrating the electromagnetic power loss density over the entire NW volume and dividing by the optical power incident on the NW. The extinction cross-section σ_{ext} is the sum of σ_{sc} and σ_{abs} , and the extinction/scattering efficiency $Q_{ext/sc}$ is the quotient of $\sigma_{ext/sc}$ and the total NW diameter.

Electric field intensity enhancement values were calculated by integrating the electric field over the nanowire cross section and dividing by the background electric field, via the formula:

$$\frac{I}{I_0} = \frac{|E|^2}{|E_0|^2} = \frac{\int (|E_x|^2 + |E_y|^2 + |E_z|^2) dA}{\int (|E_{0x}|^2 + |E_{0y}|^2 + |E_{0z}|^2) dA}$$
(5)

where E_j and E_{0j} , with j = x, y, or z, are the resonant and background electric field values, respectively, within the NW. In eigenfrequency analysis, the radiative and non-radiative Q-factors were determined according to the procedure from Christopoulos et al.⁶⁰ The Q-factors are determined by:

$$Q_{tot} = \frac{\omega_0 W}{P_{loss}} = \omega_0 W \left(\frac{1}{P_r} + \frac{1}{P_{nr}} \right), \tag{6}$$

where

$$\frac{1}{Q_{tot}} = \frac{1}{Q_r} + \frac{1}{Q_{nr}} \tag{7}$$

where ω_0 is the frequency and W is the electromagnetic mode energy localized within the NW. P_r and P_{nr} are the radiative and non-radiative components of power loss, and are analogous to the radiative and non-radiative Q-factors. P_r is calculated by integrating the Poynting vector at the scattering boundary with length l, and P_{nr} is the resistive loss within the NW. W, P_r and P_{nr} are given by:

$$W = \iint \frac{1}{4} (\varepsilon_0 \varepsilon_r |\mathbf{E}|^2 + \mu_0 |\mathbf{H}|^2) dA$$
 (8)

$$P_r = \frac{1}{2} \int Re\{E \times H^*\} \cdot \hat{\boldsymbol{n}} \, dl \tag{9}$$

$$P_{nr} = \frac{1}{2} \iint Re[\mathbf{E} \times \mathbf{J}^*] \cdot \hat{\mathbf{n}} \, dA \tag{10}$$

where ε_0 is the vacuum permittivity, ε_r is the complex permittivity, μ_0 is the vacuum permeability, \hat{n} is the unit vector, E is the electric field, H is the magnetic field, and J is the current density. This method provides a more accurate assessment of Q factor because the

default eigenfrequency calculation in FEM simulations does not account for effects such as

dispersion, so it can underestimate the value of Qtot, especially in lossy systems such as our

hybrid NWs (see Figure S8).

ASSOCIATED CONTENT

Supporting Information

Figures S1-S8, which show corresponding electric field profiles of the resonances in Figure 2B,

skin depth of Au vs. wavelength, TCMT fitting with Mie-plasmon coupling incorporated, Q-

factor and electric field plots of hybrid NWs as a function of Si core diameter, I/I_0 spectra of

select hybrid NW geometries, simulated wavelength-dependent volume-integrated electric field

of hybrid NWs of different metal and core materials, an SEM image and histogram detailing the

lengths of transferred hybrid NWs, and Q_{tot} values of a hybrid NW with varying t derived from

only the FEM solution. Tables S1-S5, which show TCMT fitting results and results from

eigenfrequency simulations.

AUTHOR INFORMATION

Corresponding Author

*Email: <u>jfcahoon@unc.edu</u>

Author contributions

J.F.C. supervised the project and secured funding. C.G.E.M synthesized the hybrid NWs,

performed SEM imaging and extinction measurements, and carried out simulations and peak

fitting. J.-S.P. formulated the TCMT analysis and developed the modifications to finite element

eigenfrequency simulations. J.F.C. and S.K. conceptualized the project, and S.K. developed the

initial procedures for hybrid NW synthesis. C.G.E.M. and J.F.C. wrote the manuscript based on

24

the input from all the authors. All authors contributed to writing and editing the manuscript.

Notes

The authors declare no competing financial interests.

ACKNOWLEDGMENT

This research was primarily supported by the National Science Foundation (NSF) through grant DMR-2121643, with foundational work supported by NSF grant DMR-1555001. This work made use of instrumentation at the Chapel Hill Analytical and Nanofabrication Laboratory (CHANL), a member of the North Carolina Research Triangle Nanotechnology Network (RTNN), which is supported by the NSF, Grant ECCS-2025064, as part of the National Nanotechnology Coordinated Infrastructure, NNCI.

REFERENCES

- 1. Cobley, C. M.; Skrabalak, S. E.; Campbell, D. J.; Xia, Y., Shape-Controlled Synthesis of Silver Nanoparticles for Plasmonic and Sensing Applications. *Plasmonics* **2009**, *4* (2), 171-179.
- 2. Sönnichsen, C.; Reinhard, B. M.; Liphardt, J.; Alivisatos, A. P., A molecular ruler based on plasmon coupling of single gold and silver nanoparticles. *Nat. Biotechnol.* **2005**, *23* (6), 741-745.
- 3. Nugroho, F. A. A.; Darmadi, I.; Cusinato, L.; Susarrey-Arce, A.; Schreuders, H.; Bannenberg, L. J.; da Silva Fanta, A. B.; Kadkhodazadeh, S.; Wagner, J. B.; Antosiewicz, T. J.; Hellman, A.; Zhdanov, V. P.; Dam, B.; Langhammer, C., Metal–polymer hybrid nanomaterials for plasmonic ultrafast hydrogen detection. *Nat. Mater.* **2019**, *18* (5), 489-495.
- 4. Mukherjee, S.; Libisch, F.; Large, N.; Neumann, O.; Brown, L. V.; Cheng, J.; Lassiter, J. B.; Carter, E. A.; Nordlander, P.; Halas, N. J., Hot Electrons Do the Impossible: Plasmon-Induced Dissociation of H2 on Au. *Nano Lett.* **2013**, *13* (1), 240-247.
- 5. Awazu, K.; Fujimaki, M.; Rockstuhl, C.; Tominaga, J.; Murakami, H.; Ohki, Y.; Yoshida, N.; Watanabe, T., A Plasmonic Photocatalyst Consisting of Silver Nanoparticles Embedded in Titanium Dioxide. *J. Am. Chem. Soc.* **2008**, *130* (5), 1676-1680.
- 6. Yan, L.; Wang, F.; Meng, S., Quantum Mode Selectivity of Plasmon-Induced Water Splitting on Gold Nanoparticles. *ACS Nano* **2016**, *10* (5), 5452-5458.
- 7. Flatae, A. M.; Tantussi, F.; Messina, G. C.; Mohammadi, A.; De Angelis, F.; Agio, M., Plasmonic Gold Nanocones in the Near-Infrared for Quantum Nano-Optics. *Advanced Optical Materials* **2017**, *5* (22), 1700586.

- 8. Shi, J.; He, X.; Chen, W.; Li, Y.; Kang, M.; Cai, Y.; Xu, H., Remote Dual-Cavity Enhanced Second Harmonic Generation in a Hybrid Plasmonic Waveguide. *Nano Lett.* **2022**, *22* (2), 688-694.
- 9. Oulton, R. F.; Sorger, V. J.; Zentgraf, T.; Ma, R.-M.; Gladden, C.; Dai, L.; Bartal, G.; Zhang, X., Plasmon lasers at deep subwavelength scale. *Nature*. **2009**, *461* (7264), 629-632.
- 10. Chang, W.-S.; Willingham, B. A.; Slaughter, L. S.; Khanal, B. P.; Vigderman, L.; Zubarev, E. R.; Link, S., Low absorption losses of strongly coupled surface plasmons in nanoparticle assemblies. *Proc. Natl. Acad. Sci.* **2011**, *108* (50), 19879.
- 11. Billaudeau, C.; Collin, S.; Pardo, F.; Bardou, N.; Pelouard, J.-L., Tailoring radiative and non-radiative losses of thin nanostructured plasmonic waveguides. *Opt. Express.* **2009**, *17* (5), 3490-3499.
- 12. Luther, J. M.; Jain, P. K.; Ewers, T.; Alivisatos, A. P., Localized surface plasmon resonances arising from free carriers in doped quantum dots. *Nat. Mater.* **2011**, *10* (5), 361-366.
- 13. Abujetas, D. R.; Paniagua-Domínguez, R.; Sánchez-Gil, J. A., Unraveling the Janus Role of Mie Resonances and Leaky/Guided Modes in Semiconductor Nanowire Absorption for Enhanced Light Harvesting. *ACS Photon.* **2015**, *2* (7), 921-929.
- 14. Kim, S.; Kim, K.-H.; Hill, D. J.; Park, H.-G.; Cahoon, J. F., Mie-coupled bound guided states in nanowire geometric superlattices. *Nat. Commun.* **2018**, *9* (1), 2781.
- 15. Kim, S.; Kim, K.-H.; Cahoon, J. F., Optical Bound States in the Continuum with Nanowire Geometric Superlattices. *Phys. Rev. Lett.* **2019**, *122* (18), 187402.
- 16. Lu, N.; Gao, A.; Dai, P.; Li, T.; Wang, Y.; Gao, X.; Song, S.; Fan, C.; Wang, Y., Ultrasensitive nucleic acids detection with electrical nanosensors based on CMOS-compatible silicon nanowire field-effect transistors. *Methods* **2013**, *63* (3), 212-218.
- 17. Yoon, J.-S.; Kim, K.; Baek, C.-K., Core-shell homojunction silicon vertical nanowire tunneling field-effect transistors. *Scientific Reports* **2017**, *7* (1), 41142.
- 18. Gao, A.; Yang, X.; Tong, J.; Zhou, L.; Wang, Y.; Zhao, J.; Mao, H.; Li, T., Multiplexed detection of lung cancer biomarkers in patients serum with CMOS-compatible silicon nanowire arrays. *Biosensors and Bioelectronics* **2017**, *91*, 482-488.
- 19. Balaghi, L.; Bussone, G.; Grifone, R.; Hübner, R.; Grenzer, J.; Ghorbani-Asl, M.; Krasheninnikov, A. V.; Schneider, H.; Helm, M.; Dimakis, E., Widely tunable GaAs bandgap via strain engineering in core/shell nanowires with large lattice mismatch. *Nat. Commun.* **2019**, *10* (1), 2793.
- 20. Bhuyan, P. D.; Kumar, A.; Sonvane, Y.; Gajjar, P. N.; Magri, R.; Gupta, S. K., Si and Ge based metallic core/shell nanowires for nano-electronic device applications. *Scientific Reports* **2018**, *8* (1), 16885.
- 21. Mokkapati, S.; Saxena, D.; Jiang, N.; Parkinson, P.; Wong-Leung, J.; Gao, Q.; Tan, H. H.; Jagadish, C., Polarization Tunable, Multicolor Emission from Core–Shell Photonic III–V Semiconductor Nanowires. *Nano Lett.* **2012**, *12* (12), 6428-6431.
- 22. Zhou, W.-X.; Chen, K.-Q., Enhancement of Thermoelectric Performance by Reducing Phonon Thermal Conductance in Multiple Core-shell Nanowires. *Scientific Reports* **2014**, *4* (1), 7150.

- 23. Guo, S.; Zhang, S.; Su, D.; Sun, S., Seed-Mediated Synthesis of Core/Shell FePtM/FePt (M = Pd, Au) Nanowires and Their Electrocatalysis for Oxygen Reduction Reaction. *J. Am. Chem. Soc.* **2013**, *135* (37), 13879-13884.
- 24. Lu, Q.; Wang, A.-L.; Gong, Y.; Hao, W.; Cheng, H.; Chen, J.; Li, B.; Yang, N.; Niu, W.; Wang, J.; Yu, Y.; Zhang, X.; Chen, Y.; Fan, Z.; Wu, X.-J.; Chen, J.; Luo, J.; Li, S.; Gu, L.; Zhang, H., Crystal phase-based epitaxial growth of hybrid noble metal nanostructures on 4H/fcc Au nanowires. *Nat. Chem.* **2018**, *10* (4), 456-461.
- 25. Velichko, E. A., Localized surface plasmon modes of core–shell bimetal nanowires do not hybridize. *Journal of the Optical Society of America A* **2020**, *37* (9), 1411-1416.
- 26. Abujetas, D. R.; Paniagua-Domínguez, R.; Nieto-Vesperinas, M.; Sánchez-Gil, J. A., Photonic band structure and effective medium properties of doubly-resonant core-shell metallo-dielectric nanowire arrays: low-loss, isotropic optical negative-index behavior. *Journal of Optics* **2015**, *17* (12), 125104.
- 27. Cheng, B.; Le, Y.; Yu, J., Preparation and enhanced photocatalytic activity of Ag@TiO2 core–shell nanocomposite nanowires. *J. Hazard. Mater.* **2010,** *177* (1), 971-977.
- 28. Mirzaei, A.; Shadrivov, I. V.; Miroshnichenko, A. E.; Kivshar, Y. S., Cloaking and enhanced scattering of core-shell plasmonic nanowires. *Opt. Express.* **2013**, *21* (9), 10454-10459.
- 29. Paniagua-Domínguez, R.; Abujetas, D. R.; Sánchez-Gil, J. A., Ultra low-loss, isotropic optical negative-index metamaterial based on hybrid metal-semiconductor nanowires. *Scientific Reports* **2013**, *3* (1), 1507.
- 30. Rothe, M.; Zhao, Y.; Kewes, G.; Kochovski, Z.; Sigle, W.; van Aken, P. A.; Koch, C.; Ballauff, M.; Lu, Y.; Benson, O., Silver nanowires with optimized silica coating as versatile plasmonic resonators. *Scientific Reports* **2019**, *9* (1), 3859.
- 31. Liu, W.; Miroshnichenko, A. E.; Oulton, R. F.; Neshev, D. N.; Hess, O.; Kivshar, Y. S., Scattering of core-shell nanowires with the interference of electric and magnetic resonances. *Opt. Lett.* **2013**, *38* (14), 2621-2624.
- 32. Aman, G.; Mohammadi, F.; Fränzl, M.; Lysevych, M.; Tan, H. H.; Jagadish, C.; Schmitzer, H.; Cahay, M.; Wagner, H. P., Effect of Au substrate and coating on the lasing characteristics of GaAs nanowires. *Scientific Reports* **2021**, *11* (1), 21378.
- 33. Hakkarainen, T.; Petronijevic, E.; Rizzo Piton, M.; Sibilia, C., Demonstration of extrinsic chirality of photoluminescence with semiconductor-metal hybrid nanowires. *Scientific Reports* **2019**, *9* (1), 5040.
- 34. Lee, H.-G.; Sai-Anand, G.; Komathi, S.; Gopalan, A.-I.; Kang, S.-W.; Lee, K.-P., Efficient visible-light-driven photocatalytic degradation of nitrophenol by using graphene-encapsulated TiO2 nanowires. *J. Hazard. Mater.* **2015**, *283*, 400-409.
- 35. Agarwal, D.; Aspetti, C. O.; Cargnello, M.; Ren, M.; Yoo, J.; Murray, C. B.; Agarwal, R., Engineering Localized Surface Plasmon Interactions in Gold by Silicon Nanowire for Enhanced Heating and Photocatalysis. *Nano Lett.* **2017**, *17* (3), 1839-1845.
- 36. Fan, P.; Chettiar, U. K.; Cao, L.; Afshinmanesh, F.; Engheta, N.; Brongersma, M. L., An invisible metal–semiconductor photodetector. *Nat. Photon.* **2012**, *6* (6), 380-385.

- 37. Lin, N.; Zhang, W.; Koshel, B. M.; Cheng, J.-X.; Yang, C., Spatially Modulated Two-Photon Luminescence from Si–Au Core–Shell Nanowires. *J. Phys. Chem. C* **2011**, *115* (8), 3198-3202.
- 38. Park, J.-S.; Kim, K.-H.; Hwang, M.-S.; Zhang, X.; Lee, J. M.; Kim, J.; Song, K.-D.; No, Y.-S.; Jeong, K.-Y.; Cahoon, J. F.; Kim, S.-K.; Park, H.-G., Enhancement of Light Absorption in Silicon Nanowire Photovoltaic Devices with Dielectric and Metallic Grating Structures. *Nano Lett.* **2017**, *17* (12), 7731-7736.
- 39. Glassner, S.; Keshmiri, H.; Hill, D. J.; Cahoon, J. F.; Fernandez, B.; den Hertog, M. I.; Lugstein, A., Tuning Electroluminescence from a Plasmonic Cavity-Coupled Silicon Light Source. *Nano Lett.* **2018**, *18* (11), 7230-7237.
- 40. Ren, M.-L.; Liu, W.; Aspetti, C. O.; Sun, L.; Agarwal, R., Enhanced second-harmonic generation from metal-integrated semiconductor nanowires via highly confined whispering gallery modes. *Nat. Commun.* **2014**, *5* (1), 5432.
- 41. Guo, H.; Hu, Q.; Zhang, C.; Liu, H.; Wu, R.; Pan, S., Strong Plasmon-Mie Resonance in Si@Pd Core-Ω Shell Nanocavity. *Materials* **2023**, *16* (4), 1453.
- 42. Bardhan, R.; Grady, N. K.; Ali, T.; Halas, N. J., Metallic Nanoshells with Semiconductor Cores: Optical Characteristics Modified by Core Medium Properties. *ACS Nano* **2010**, *4* (10), 6169-6179.
- 43. E. Prodan, C. R., N.J. Halas, P. Nordlander, A Hybridization Model for the Plasmon Response of Complex Nanostructures. *Science*. **2003**, *302* (5644), 419-422.
- 44. Kim, S.; Hill, D. J.; Pinion, C. W.; Christesen, J. D.; McBride, J. R.; Cahoon, J. F., Designing Morphology in Epitaxial Silicon Nanowires: The Role of Gold, Surface Chemistry, and Phosphorus Doping. *ACS Nano* **2017**, *11* (5), 4453-4462.
- 45. La Parola, V.; Testa, M. L.; Venezia, A. M., Pd and PdAu catalysts supported over 3-MPTES grafted HMS used in the HDS of thiophene. *Applied Catalysis B: Environmental* **2012**, *119-120*, 248-255.
- 46. Chen, J.-J.; Struk, K. N.; Brennan, A. B., Surface Modification of Silicate Glass Using 3- (Mercaptopropyl)trimethoxysilane for Thiol–Ene Polymerization. *Langmuir* **2011**, *27* (22), 13754-13761.
- 47. Mondin, G.; Lohe, M. R.; Wisser, F. M.; Grothe, J.; Mohamed-Noriega, N.; Leifert, A.; Dörfler, S.; Bachmatiuk, A.; Rümmeli, M. H.; Kaskel, S., Electroless copper deposition on (3-mercaptopropyl)triethoxysilane-coated silica and alumina nanoparticles. *Electrochim. Acta* **2013**, *114*, 521-526.
- 48. Gothe, P. K.; Gaur, D.; Achanta, V. G., MPTMS self-assembled monolayer deposition for ultra-thin gold films for plasmonics. *Journal of Physics Communications* **2018**, *2* (3), 035005.
- 49. Celano, T. A.; Kim, S.; Hill, D. J.; Cahoon, J. F., Semi-transparent, flexible, and electrically conductive silicon mesh by capillarity-driven welding of vapor-liquid-solid-grown nanowires over large areas. *Nano Res.* **2020**, *13* (5), 1465-1471.
- 50. Schinke, C.; Christian Peest, P.; Schmidt, J.; Brendel, R.; Bothe, K.; Vogt, M. R.; Kröger, I.; Winter, S.; Schirmacher, A.; Lim, S.; Nguyen, H. T.; MacDonald, D., Uncertainty analysis for the coefficient of band-to-band absorption of crystalline silicon. *AIP Advances* **2015**, *5* (6), 067168.

- 51. Bohren, C. F. H., Donald R., *Absorption and Scattering of Light by Small Particles*. Wiley: New York, 1998.
- 52. Rybin, M. V.; Samusev, K. B.; Sinev, I. S.; Semouchkin, G.; Semouchkina, E.; Kivshar, Y. S.; Limonov, M. F., Mie scattering as a cascade of Fano resonances. *Opt. Express.* **2013**, *21* (24), 30107-30113.
- 53. Fan, P.; Yu, Z.; Fan, S.; Brongersma, M. L., Optical Fano resonance of an individual semiconductor nanostructure. *Nat. Mater.* **2014**, *13* (5), 471-475.
- 54. Ruan, Z.; Fan, S., Temporal Coupled-Mode Theory for Fano Resonance in Light Scattering by a Single Obstacle. *J. Phys. Chem. C* **2010**, *114* (16), 7324-7329.
- 55. Ruan, Z.; Fan, S., Superscattering of Light from Subwavelength Nanostructures. *Phys. Rev. Lett.* **2010**, *105* (1), 013901.
- 56. Lilley, G.; Messner, M.; Unterrainer, K., Improving the quality factor of the localized surface plasmon resonance. *Optical Materials Express* **2015**, *5* (10), 2112-2120.
- 57. Kim, Y.-H.; Kwon, S.-H.; Ee, H.-S.; Hwang, Y.; No, Y.-S.; Park, H.-G., Dependence of Q Factor on Surface Roughness in a Plasmonic Cavity. *J. Opt. Soc. Korea* **2016**, *20* (1), 188-191.
- 58. Qin, L.; Zhang, C.; Li, R.; Li, X., Silicon-gold core-shell nanowire array for an optically and electrically characterized refractive index sensor based on plasmonic resonance and Schottky junction. *Opt. Lett.* **2017**, *42* (7), 1225-1228.
- 59. Teitsworth, T. S.; Hill, D. J.; Litvin, S. R.; Ritchie, E. T.; Park, J.-S.; Custer, J. P.; Taggart, A. D.; Bottum, S. R.; Morley, S. E.; Kim, S.; McBride, J. R.; Atkin, J. M.; Cahoon, J. F., Water splitting with silicon p—i—n superlattices suspended in solution. *Nature*. **2023**, *614* (7947), 270-274.
- 60. Christopoulos, T.; Tsilipakos, O.; Sinatkas, G.; Kriezis, E. E., On the calculation of the quality factor in contemporary photonic resonant structures. *Opt. Express.* **2019**, *27* (10), 14505-14522.

For Table of Contents Only

